J Arid Land (2025) 17(4): 440–456
doi: 10.1007/s40333-025-0077-8; CSTR: 32276.14.JAL.02500778

Science Press Springer-Verlag

Response of precipitation isotopes and water vapor sources to regional climate change on the Gannan Plateau, China

CHEN Fenli[1,2*], KANG Nan[1,2], WANG Shengjie[1,2], GAO Minyan[1,2], ZHANG Qiuyan[1,2], LI Huizhen[1,2], YAO Yiwen[1,2]

[1] College of Geography and Environmental Science, Northwest Normal University, Lanzhou 730070, China;
[2] Key Laboratory of Resource Environment and Sustainable Development of Oasis of Gansu Province, Northwest Normal University, Lanzhou 730070, China

Abstract: Precipitation isotopes ($\delta^{18}O$ and $\delta^{2}H$) are closely related to meteorological conditions for precipitation generation and the initial state of water vapor source areas, and are essential to the study of the regional hydrological cycle. The deuterium excess (*d*-excess) indicates deviation in isotope fractionation during evaporation and can trace water vapor sources. This study analyzed 443 precipitation samples collected from the Gannan Plateau, China in 2022 to assess precipitation isotope variations and their driving factors. Water vapor sources were evaluated using the Hybrid Single-Particle Lagrangian Integrated Trajectory (HYSPLIT), Concentration Weighted Trajectory (CWT), and Potential Source Contribution Factor (PSCF) models. Results showed that precipitation isotope values showed significant spatial and temporal variations on the Gannan Plateau. Temporally, precipitation isotope values peaked in June (when evaporation dominated) and minimized in March (depletion effect of air masses in the westerly wind belt). Spatially, the isotope values showed a distribution pattern of "high in the east and low in the west", which was mainly regulated by the differences in altitude and local meteorological conditions. Compared with the global meteoric water line (GMWL) with equation of $\delta^{2}H=8.00\delta^{18}O+10.00$, the slope and intercept of local meteoric water line (LMWL) for precipitation on the Gannan Plateau were smaller (7.49 and 7.63, respectively), reflecting the existence of a stronger secondary evaporation effect under the clouds in the region. The sources of water vapor on the Gannan Plateau showed significant seasonality and spatial heterogeneity. Specifically, the westerly belt and monsoon were the main water vapor transport paths at each sampling point, with Central Asian continental water vapor dominating in spring (53.49%), Indian Ocean water vapor dominating in summer (52.53%), Atlantic Ocean water vapor dominating in autumn (46.74%), and Atlantic Ocean and Mediterranean Sea water vapor dominating in winter (42.30% and 33.68%, respectively). Changes in the intensity of convective activity and Outgoing Longwave Radiation (OLR) affected the enrichment of isotopic values, which exhibited the same change trends as $\delta^{18}O$. During the precipitation process, the $\delta^{18}O$ value first decreased and then increased. During the initial and final stages of precipitation process, precipitation was mainly influenced by continental air masses, while during the middle stage, it was controlled by marine air masses. The systematic research on precipitation isotopes and water vapor sources is important for climate change research and extreme precipitation prediction on the Gannan Plateau and other similar areas.

Keywords: precipitation isotopes; deuterium excess (*d*-excess); water vapor sources; Hybrid Single-Particle Lagrangian Integrated Trajectory (HYSPLIT); Concentration Weighted Trajectory (CWT); Potential Source Contribution Factor (PSCF); Gannan Plateau

*Corresponding author: CHEN Fenli (E-mail: chenfenli1102@163.com)
Received 2024-09-05; revised 2024-12-28; accepted 2025-01-03

Citation: CHEN Fenli, KANG Nan, WANG Shengjie, GAO Minyan, ZHANG Qiuyan, LI Huizhen, YAO Yiwen. 2025. Response of precipitation isotopes and water vapor sources to regional climate change on the Gannan Plateau, China. Journal of Arid Land, 17(4): 440–456. https://doi.org/10.1007/s40333-025-0077-8; https://cstr.cn/32276.14.JAL.02500778

1 Introduction

Atmospheric precipitation plays a crucial role in the groundwater–soil–plant–atmosphere continuum (GSPAC) system, linking the atmosphere and hydrosphere and enabling material and energy exchange between them. Stable isotopes of $\delta^{18}O$ and $\delta^{2}H$, though minor components of water, are highly sensitive to environmental changes and serve as natural tracers. Their composition in precipitation reveals the sources and transport of water vapor, as well as environmental changes, and is crucial for studying global precipitation and the dynamics of water vapor in atmospheric dynamical systems. As tracers, they can track the movement of water vapor, precisely locate the sources, pathways, and exchanges between media of water, thereby influencing water balance and ecological functions (Zhang et al., 2021). They are also activators in water bodies and have a close connection with the meteorological processes resulting in precipitation. Since isotope fractionation changes the original $\delta^{18}O$ and $\delta^{2}H$ of water vapor, stable isotope compositions in different water bodies display both universal and divergent characteristics. During the global-scale hydrological cycle, isotope fractionation occurs through evaporation and condensation, leading to a linear relationship expressed as: $\delta^{2}H=8.00\delta^{18}O+10.00$. This equation represents the typical pattern of linear correlation between $\delta^{2}H$ and $\delta^{18}O$ in precipitation and the fitted line is commonly referred to as the global meteoric water line (GMWL) (Craig, 1961). The deuterium excess (*d*-excess) represents the isotopic composition of water vapor over a local area under dynamical fractionation, reflecting the degree of imbalance in the evaporation and condensation process at the sources of water vapor. Furthermore, it is a crucial indicator for tracing the water vapor sources and calculating the extent that the local meteoric water line (LMWL) deviates from the GMWL (Dansgaard, 1964).

Precipitation isotope fluctuations are closely related to the drivers and controls of large-scale atmospheric circulation patterns, such as water vapor sources, transport processes, water vapor interactions, and local water cycle mechanisms. Long-term observations of stable isotopes in precipitation can be used as a complementary tool to examine precipitation processes in different periods and can also be used to identify the sources of water vapor. Some scholars have used Potential Source Contribution Factor (PSCF) and Concentration Weighted Trajectory (CWT) methods to quantify the contribution rates of potential water vapor source areas to precipitation, which further improves the accuracy and applicability of stable isotopes in water vapor source analysis (Ara Begum et al., 2005; Meng et al., 2020a).

Previous studies have confirmed that water vapor in Northwest China mainly consists of evapotranspiration from the Asian-European continent (Shi et al., 2021), westerly airflow from the Atlantic Ocean (Zhang et al., 2019), southwesterly oceanic airflow from the Bay of Bengal (Wang et al., 2005), and warm humid airflow from the western Pacific Ocean (Wei et al., 2010). Current research of precipitation isotopes in Northwest China mainly focuses on relatively large-scale basins such as the Tarim River Basin (Meng et al., 2020b), Heihe River Basin (Song et al., 2022), and Shiyang River Basin (Zhao et al., 2019). However, relatively few studies have been conducted on small-scale monsoon-influenced alpine regions, which are crucial for regulating climate and conserving water. In recent years, the climate has begun to transform to warm and humid, and the special topography and ecological environment conditions have greatly increased the frequency of extreme precipitation events on the Gannan Plateau, China (Zhao et al., 2023). Research has shown that the daily precipitation intensity, number of days of heavy precipitation, and annual precipitation changes on the Gannan Plateau showed an upward trend (Wei et al., 2023). This led to secondary disasters that have hampered the sustainable growth of grassland animal husbandry on the Gannan Plateau and greatly threatened the ecological security and water supplies of the Yellow River Basin, China. Therefore, this study selected five meteorological stations (serving as sampling points) on the Gannan Plateau to systematically

analyze the spatiotemporal distribution characteristics of precipitation isotopes and their correlation with meteorological factors. Meanwhile, we constructed the LMWL equations for each sampling point to identify the water vapor sources on the Gannan Plateau during different periods and quantify the amount that each water vapor source contributes to precipitation. The findings can offer scientific basis for subsequent extreme precipitation and disaster prevention on the Gannan Plateau and provide suggestions and support for the study of hydrological processes of the microclimates in similar areas.

2 Materials and methods

2.1 Study area

Gannan Plateau (Fig. 1) is located on the eastern edge of the Qinghai–Xizang Plateau and is an important water supply area for the upper reaches of the Yellow River, China. The terrain is high in the west and low in the east; the landform is complex and diverse, and can be generally divided into three parts: the western alpine grassland area, the eastern hilly mountain area, and the southern Mindie Mountain area. The plateau belongs to an alpine continental climate with low temperature and strong light. Rain and heat coexist at the same time, and precipitation is mainly concentrated in summer and autumn. To identify the variation characteristics of temperature and precipitation on the Gannan Plateau, we analyzed historical meteorological data spanning from 1981 to 2020. The results showed that during 1981–2020, the average annual temperature was 4.3℃, the coldest average temperature in January was –6.3℃, and the hottest average temperature in July was 15.6℃. The average annual precipitation was 421.4 mm, and the precipitation in the wet season (April–October) accounted for 77.00% of the annual precipitation.

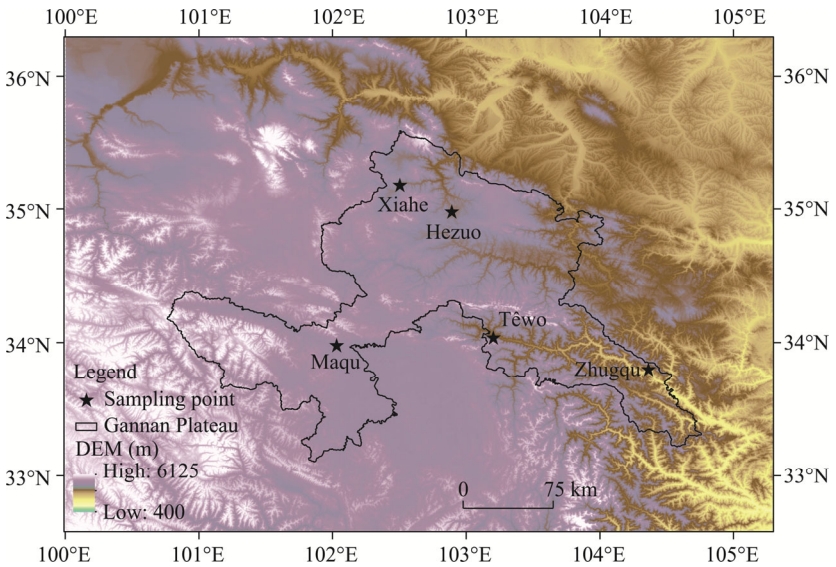

Fig. 1 Overview of the Gannan Plateau based on the digital elevation model (DEM) and distribution of the five precipitation sampling points

2.2 Sample collection and measurement

This study collected a total of 443 precipitation event samples, comprehensively covering all months of the year 2022 at five meteorological stations (Maqu, Hezuo, Têwo, Zhugqu, and Xiahe) within the study area (Table 1). Precipitation was collected using a standard funnel-type rain barrel. To avoid the effects of evaporation on precipitation, precipitation samples were timely packed into 50 mL HDPE plastic bottles at the end of each precipitation event. Solid precipitation samples were first placed in a sealed plastic bag to allow it to melt naturally at room temperature and then

deposited into the sampling bottles. The $\delta^{18}O$ and $\delta^{2}H$ of samples were measured using the liquid water isotope analyzer DLT–100 (Los Gatos Research, Mountain View, San Jose, CA, USA) in the stable isotope laboratory of College of Geography and Environmental Science, Northwest Normal University, China. Each sample was measured six times in order to prevent the injection memory effect. The final result of the samples was determined by taking the average value of the last four injection. The accuracies of the measurements of $\delta^{18}O$ and $\delta^{2}H$ were ±0.20‰ and ±0.60‰, respectively. The $\delta^{18}O$ and $\delta^{2}H$ of the samples were expressed conventionally as δ_{sample} (‰), which represents the deviations per mil (‰) from the Vienna Standard Mean Ocean Water (VSMOW) for ^{18}O and ^{2}H, and the formula is as follows:

$$\delta_{\text{sample}} = \frac{R_{\text{sample}}}{R_{\text{standard}}} - 1, \tag{1}$$

where R_{sample} is the ratio of $^{18}O/^{16}O$ (or $^{2}H/^{1}H$) in precipitation samples; and $R_{standard}$ is the corresponding isotope ratio in VSMOW.

Long-term meteorological data (1981–2020) were used to describe the climate conditions in the study area. The hourly ground data of the five meteorological stations from January to December 2022 were selected to provide meteorological characteristics including temperature, precipitation, and relative humidity for the precipitation samples. The long-term meteorological data and hourly ground data for the study area were obtained from the China Meteorological Data Network (https://data.cma.cn/). Outgoing longwave radiation (OLR) data at a spatial resolution of 2.5°×2.5° were obtained from the University of Maryland (UMD) OLR Climate Data Record (CDR) (http://olr.umd.edu/) for analyzing its correlation with precipitation isotope $\delta^{18}O$.

Table 1 Basic information of precipitation sampling points on the Gannan Plateau

Sampling point	Latitude	Longitude	Altitude (m)	Number of samples	Annual climatology		
					Temperature (℃)	Precipitation (mm)	Relative humidity (%)
Maqu	34°00′N	102°05′E	3471	84	8.8	494.5	76.8
Hezuo	35°00′N	102°54′E	2910	141	7.7	448.8	79.4
Têwo	34°04′N	103°14′E	2374	78	10.6	436.6	77.4
Zhugqu	33°47′N	104°22′E	1400	74	17.6	350.5	72.8
Xiahe	35°21′N	102°53′E	2229	66	7.4	374.2	73.8

2.3 Methods

2.3.1 Calculation method for annual and monthly weighted average of precipitation isotopes

The annual and monthly weighted average precipitation isotopes are expressed as:

$$\delta = \frac{\sum \delta_l \times P_l}{\sum P_l}, \tag{2}$$

where δ is the weighted average of $\delta^{18}O$ (or $\delta^{2}H$) in precipitation (‰); P_l is the amount of precipitation for the precipitation event l (mm); and δ_l is the corresponding isotope value of precipitation for the precipitation event l (‰).

The *d*-excess (‰) was used to describe the isotopic composition characteristics of H and O in water bodies. It is the intercept when the slope of the LMWL ($\delta^{2}H/\delta^{18}O$) is 8.00, and serves as an indication of the degree of imbalance in the evaporation process. The formula is as follows:

$$d\text{-excess} = \delta^{2}H - 8\delta^{18}O. \tag{3}$$

2.3.2 Hybrid Single-Particle Lagrangian Integrated Trajectory (HYSPLIT) analysis

In this study, the backward trajectory model was used to identify water vapor sources and transport paths. Since water vapor is mainly concentrated in the troposphere, the height of the starting point of the trajectory calculation was set at 1500 m above ground level, and its corresponding air pressure surface was about 850 hPa. The water vapor migration trajectory calculation was carried

out in the troposphere four times a day (00:00, 06:00, 12:00, and 18:00 Coordinated Universal Time (UTC)) at 6-h intervals. The model hindcast time was set to 240 h based on the average residence time (8–9 d) of precipitating air masses in the atmosphere. Finally, the cluster analysis tool Trajstat in the HYSPLIT model was used to merge similar water vapor migration trajectories (Wang, 2014; Sun et al., 2023).

2.3.3 PSCF analysis

In this study, the PSCF method was used to analyze and determine the geographic location and spatial distribution of potential water vapor source areas based on a conditional probability function combined with water vapor *d*-excess value of the air mass trajectory. The main principle is to divide the study area into several grids of 1°×1° and take the monthly average water vapor *d*-excess value as the threshold. The air mass trajectory with water vapor *d*-excess value exceeding the set threshold when reaching the research point is defined as the trajectory with strong evaporation, and the corresponding area of the trajectory is the potential water vapor source area of the research point. The formula is expressed as:

$$\mathrm{PSCF}_{ij} = \frac{m_{ij}}{n_{ij}}, \tag{4}$$

where PSCF_{ij} is the conditional probability of grid (i, j); m_{ij} is the number of trajectories passing through grid (i, j) with water vapor *d*-excess values exceeding a set threshold; and n_{ij} is the total number of trajectories passing through grid (i, j). When n_{ij} is too small, deviation will occur. To reduce the error produced in the calculation, we introduced a weight factor $\mathrm{W}(n_{ij})$ to calculate the weighted conditional probability (WPSCF_{ij}), and the formulas are as follows (Wang et al., 2006):

$$\mathrm{WPSCF}_{ij} = \mathrm{PSCF}_{ij} \times \mathrm{W}\left(n_{ij}\right), \tag{5}$$

$$\mathrm{W}\left(n_{ij}\right) = \begin{cases} 1.00 & \text{if } 80 < n_{ij} \\ 0.70 & \text{if } 20 < n_{ij} \le 80 \\ 0.42 & \text{if } 10 < n_{ij} \le 20 \\ 0.05 & \text{if } n_{ij} \le 10 \end{cases}. \tag{6}$$

2.3.4 CWT analysis

PSCF can only judge the scope of the potential water vapor source areas, but cannot clarify the specific contribution rates of different air mass trajectories. Therefore, the CWT analysis was introduced in this study to calculate the specific contribution rates of potential water vapor source areas. The CWT analysis draws on NOAA's reanalysis data and uses Meteinfo software to generate 10-d backward trajectories for the research point. By calculating the average water vapor *d*-excess value when different trajectories pass through the grid (i, j), we identified the contribution rate of the potential water vapor source area of the research point. The formulas are expressed as:

$$\mathrm{C}_{ij} = \frac{\sum_{k=1}^{m_{ij}} \mathrm{C}_k \, \mathrm{T}_{ijk}}{\sum_{k=1}^{m_{ij}} \mathrm{T}_{ijk}}, \tag{7}$$

$$\mathrm{WCWT}_{ij} = \mathrm{C}_{ij} \times \mathrm{W}\left(n_{ij}\right), \tag{8}$$

where C_{ij} is the average weighted water vapor *d*-excess value on grid (i, j) (‰/m^3); C_k is the corresponding water vapor *d*-excess value of the trajectory k passing through grid (i, j); T_{ijk} is the residence time of the trajectory k on the grid (i, j) and is replaced by the number of endpoints of the trajectory that fall within the grid in the calculation process; and WCWT_{ij} is the weighted C_{ij} used to reduce the error produced in the calculation.

3 Results and discussion

3.1 Spatiotemporal variation characteristics of precipitation isotopes

The precipitation isotope values in the study area can be divided into low-high-low phases in 2022 (Fig. 2a). $\delta^{18}O$ correlated well with $\delta^{2}H$ due to isotope fractionation. $\delta^{18}O$ and $\delta^{2}H$ were enriched in summer and autumn and depleted in winter and spring, but the overall fluctuation was small. The monthly weighted average $\delta^{18}O$ and $\delta^{2}H$ values were largest in June and smallest in February (Fig. 2b). Compared with the other months, the isotope values showed obvious depletion in February. However, there were increasing trends of $\delta^{18}O$ and $\delta^{2}H$ at the end of February and the beginning of March, which may be related to the influence of water vapor sources and local environment.

The spatial variation in precipitation isotopes indicated an overall increasing trend from west to east (Fig. 2c and d). The terrain in the study area is higher in the west and lower in the east. The precipitation isotope values decreased with increasing altitude. The maximum values of $\delta^{18}O$ and $\delta^{2}H$ both occurred at Zhugqu, which were –4.42‰ and –28.83‰, respectively, while the lowest values of $\delta^{18}O$ (–10.57‰) and $\delta^{2}H$ (–78.08‰) were found at Maqu.

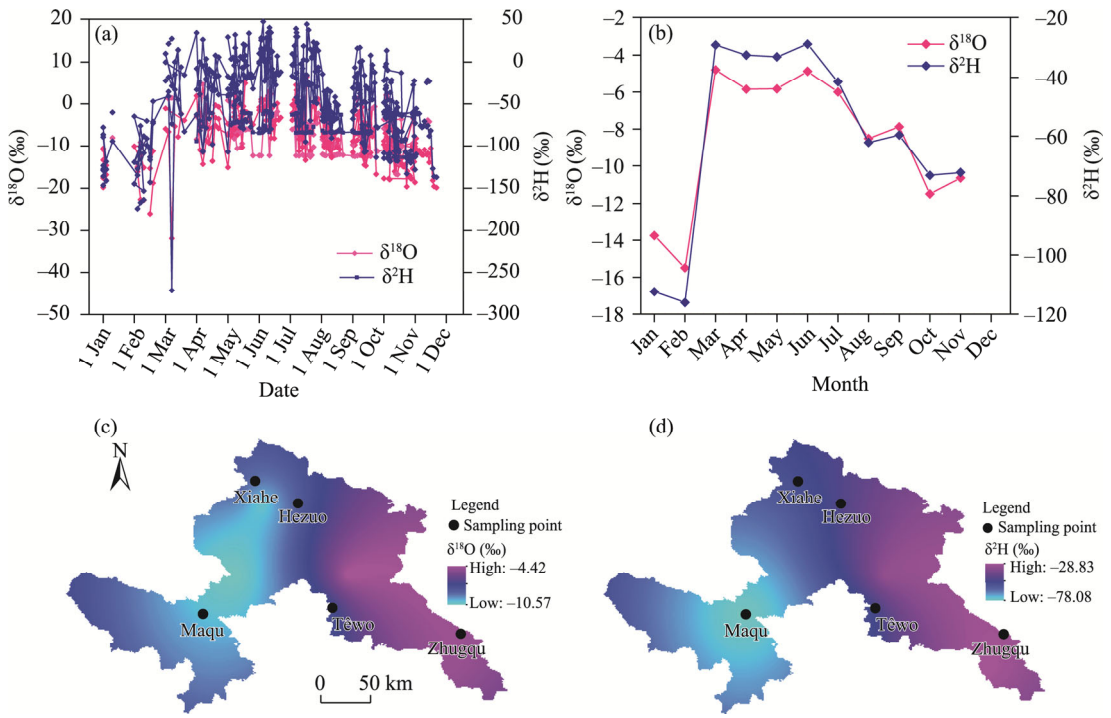

Fig. 2 Spatiotemporal variation characteristics of precipitation isotopes on the Gannan Plateau. (a), temporal variation in event-based precipitation isotopes; (b), temporal variation in monthly weighted average precipitation isotopes; (c), spatial variation in annual weighted average $\delta^{18}O$; (d), spatial variation in annual weighted average $\delta^{2}H$.

The *d*-excess values exhibited an overall three-stage characteristic of high-low-high from April to December 2022 at different sampling points across the Gannan Plateau (Fig. 3). Specifically, the *d*-excess values were relatively high in spring and winter and relatively low in summer and autumn, with an overall small fluctuation. The maximum *d*-excess value occurred in February, and the minimum occurred in October. At Hezuo, the *d*-excess values ranged from –16.20‰ to 77.91‰, with an average of 18.43‰; while at Têwo, the *d*-excess values ranged from –20.11‰ to 26.25‰, with an average of 11.47‰. Notably, except for the two sampling points (Hezuo and Têwo), the average *d*-excess values at other sampling points were all below the global average

(10.00‰). This phenomenon indicated that the impact of sub-cloud secondary evaporation on the Gannan Plateau was significant and cannot be ignored.

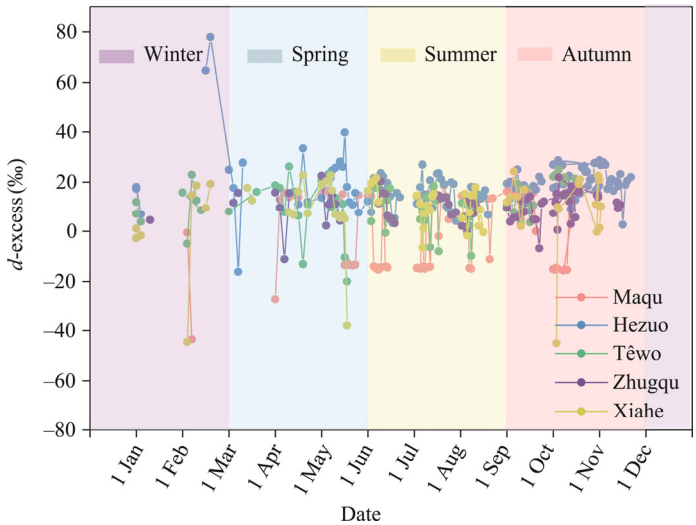

Fig. 3 Temporal variation characteristics of deuterium excess (*d*-excess) at different sampling points across the Gannan Plateau

3.2 Relationship between $\delta^{18}O$ and $\delta^{2}H$ of precipitation

By utilizing the stable isotope values from precipitation events spanning January to December 2022, we fitted the LMWL for precipitation on the Gannan Plateau as: $\delta^{2}H=7.49\delta^{18}O+7.63$ (Fig. 4a). The slope and intercept were comparatively low when juxtaposed with the GMWL equation ($\delta^{2}H=8.00\delta^{18}O+10.00$), indicating that relative humidity in this region was minimal and there was limited exchange between liquid water and vapor (Chen et al., 2022b; Zhang et al., 2024). During its descent, precipitation experienced a degree of secondary evaporation, leading to an enrichment of heavy isotopes, which resulted in a reduction of both the slope and intercept of LMWL of precipitation (Zhou et al., 2020). Figure 4b presents a comparison of LMWL for precipitation across various sampling points on the Gannan Plateau. The slopes ranged from 5.15 to 7.70 and the intercepts varied from –23.37 to 15.65. The discrepancies observed in both slope and intercept values for LMWL at each sampling point reflected variations in sources of water vapor as well as

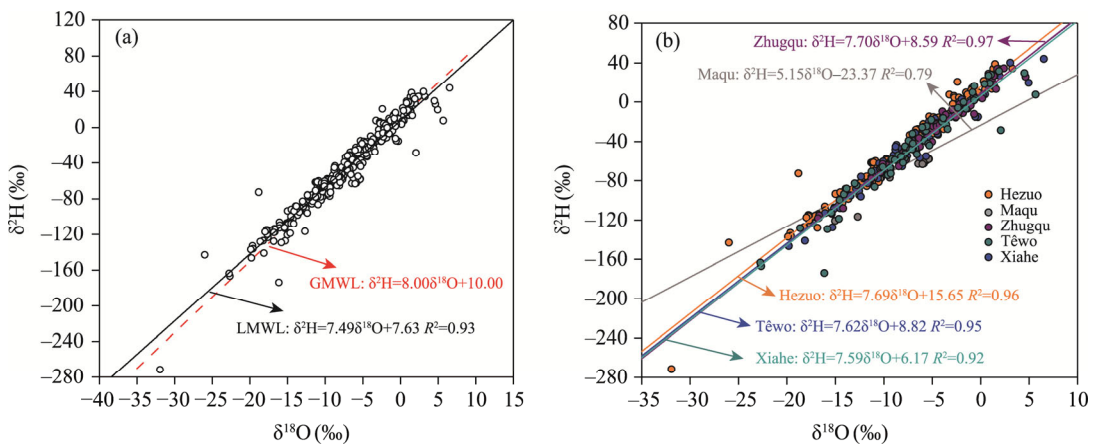

Fig. 4 Comparison between GMWL and LMWL based on all precipitation events on the Gannan Plateau (a) and among the LMWLs based on the precipitation events at each sampling point (b). GMWL, global meteoric water line; LMWL, local meteoric water line.

local hydrological cycles (Tian et al., 2001). Notably, Maqu exhibited the lowest intercept and slope of LMWL due to its arid climate characterized by low relative humidity, which fosters pronounced secondary evaporation and significant isotope fractionation (Chen et al., 2022a). Conversely, Zhugqu displayed a higher slope value than other sampling points potentially attributable to its geographic positioning (Liu and Wang, 2023). Zhouqu, which is situated within the southern Qinling Mountains of China with abundant plant resources, demonstrated elevated relative humidity that resulted in an increased slope of LMWL compared with other sampling points (Li et al., 2022).

3.3 Regional water vapor sources and their contribution proportions

The seasonal variations in precipitation isotopes are related to water vapor sources (Huang et al., 2017; Kohfahl et al., 2021). Subsequently, this study explored the relationship between precipitation isotopes and water vapor sources for each season in 2022 by cluster analysis of simulated trajectories (Fig. 5). In spring, the water vapor was supplied by the western part of the study area and was continuously pushed eastward by the westerly circulation (Fig. 5a1). The cluster analysis showed that about 53.49% of the water vapor came from the Central Asian continent in the northwest, 36.41% from the Mediterranean Sea, and 10.10% from the Atlantic Ocean (Fig. 5a2). In summer, the sources of water vapor were diverse and complex; there was inland water vapor transported by a westerly wind, ocean water vapor transported by South Asian monsoon, and local circulating water vapor formed by evaporation during this period (Fig. 5b1). Figure 5b2 shows that about 52.53% of water vapor was from the Indian Ocean, 25.82% from the Central Asian continent, and 21.65% from the Mediterranean Sea. In autumn, the water vapor mainly came from the westerly wind belt and near-source local evaporation (Fig. 5c1). Specifically, 46.74% of the water vapor was the Atlantic Ocean water vapor, 32.66% was influenced by local evaporative water vapor, and the remaining 20.60% was mainly formed by the Mediterranean water vapor (Fig. 5c2). In winter, the water vapor on the Gannan Plateau was mainly transported eastward under the influence of the westerly belt (Fig. 5d1). The cluster analysis of air mass trajectories showed that 42.30% of the water vapor was Atlantic water vapor, 33.68% was Mediterranean water vapor, and 24.02% was from continental dry air mass (Fig. 5d2).

In summary, the investigation into the sources of water vapor on the Gannan Plateau aligns with prior research findings in Northwest China (Wu et al., 2021; Yang et al., 2022), indicating a significant influence from westerly circulation and diverse origins of water vapor. However, notable disparities existed regarding the extent of westerly circulation's impact and the contribution rates of various water vapor sources across different regions. For instance, due to its enclosed topography, the Tarim River Basin primarily acquires water vapor through low-lying passes or valleys to the west, resulting in comparatively lower levels of water vapor content (Song et al., 2022). Conversely, in the Heihe River Basin, most water vapor was sourced from both the Atlantic Ocean and Arctic Ocean and was predominantly transported in a west-to-east latitudinal trajectory (Meng et al., 2020a). The Shiyang River Basin exhibited relatively more intricate sources of water vapor; the water vapor was not only influenced by terrestrial contributions from Central Asia, Mongolia-Siberia, Europe, and inland China but also augmented by oceanic inputs from the Atlantic Ocean, Pacific Ocean, and Indian Ocean (Yuan et al., 2020). The climate change on the Gannan Plateau is significantly affected by the high pressure systems of Qinghai–Xizang Plateau; when this high pressure shifts northward, southern airflow on its western flank intensifies, facilitating moisture transport from the Bay of Bengal to this plateau. Consequently, while primary water vapor sources remained relatively stable, mainly comprising inland moisture conveyed by westerly winds alongside oceanic contributions, the addition of monsoonal moisture during summer and autumn as well as local circulatory influences further enriched these hydrological resources.

3.4 Roles of local meteorological conditions and large-scale atmospheric circulation in modulating precipitation isotope distribution

The $\delta^{18}O$ and $\delta^{2}H$ exhibit regular characteristics as they vary with environmental factors or

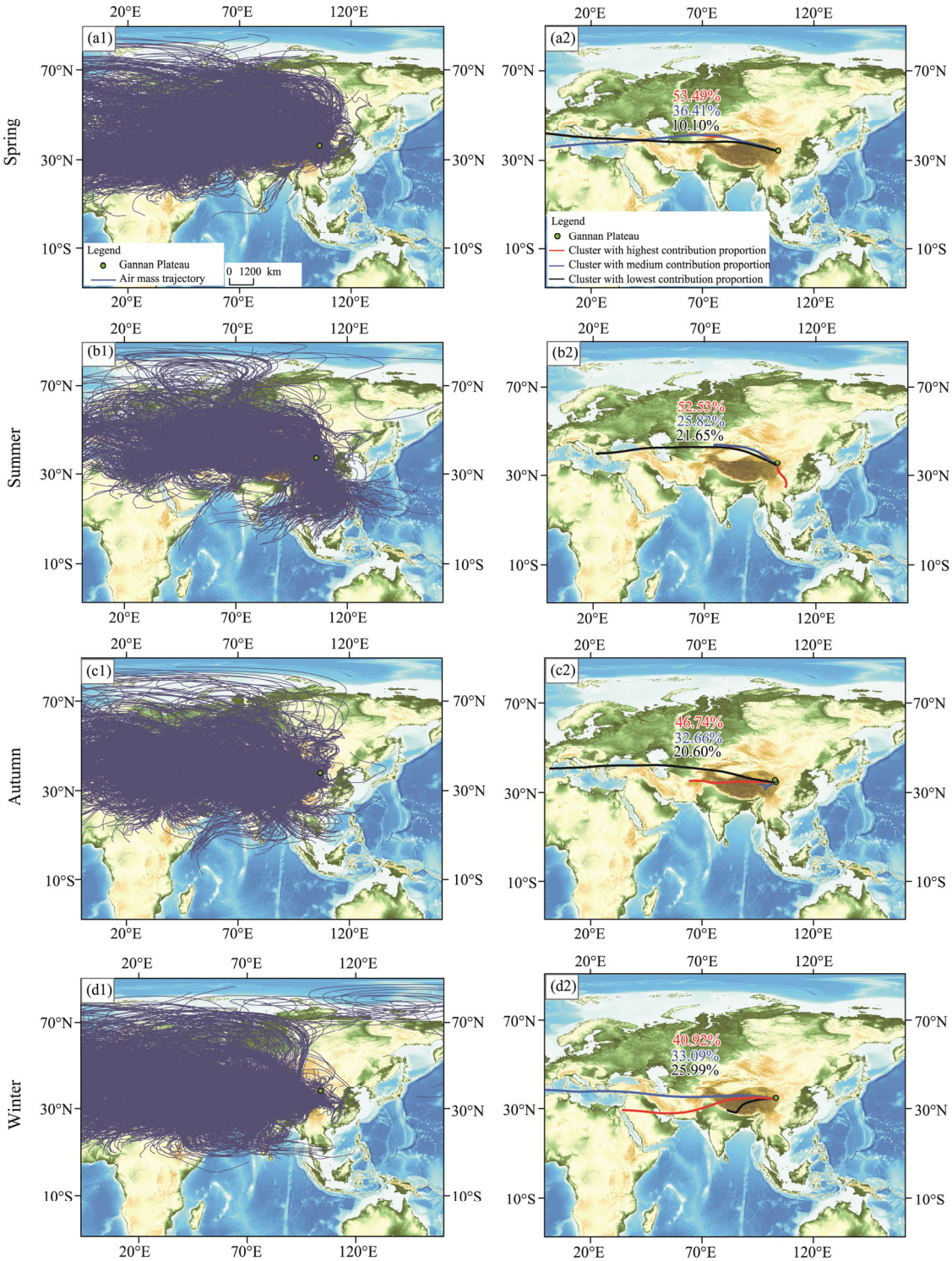

Fig. 5 Air mass trajectories (a1–d1) and their clustering results (a2–d2) for each season in 2022. Note that the base map used was obtained from the National Centers for Environmental Information website (https://www.ncei.noaa.gov/products/etopo-global-relief-model).

climatic parameters (Yu and Li, 2018). They play a crucial role as markers in the water cycle, capable of conveying abundant hydrological information, including the sources of water vapor, sub-cloud secondary evaporation, and water vapor recycling (Zhang and Wang, 2016). The strong

spatial variability of precipitation isotopes on the Gannan Plateau may be related to local meteorological factors, including precipitation, temperature, and relative humidity, as well as the choice of sampling points (Liu et al., 2009). Therefore, this paper delved into the correlations of $\delta^{18}O$ and *d*-excess with temperature, precipitation, and relative humidity (Fig. 6).

We could clearly observe a significant correlation between $\delta^{18}O$ and temperature (R^2=0.16, P<0.01) and between *d*-excess and temperature (R^2=0.04, P<0.01). As temperature raised, $\delta^{18}O$ showed an increasing trend, while *d*-excess exhibited a decreasing trend. A negative correlation was observed between $\delta^{18}O$ and precipitation (R^2=0.01, P=0.05), indicating that as precipitation increased, $\delta^{18}O$ decreased. In contrast, the *d*-excess showed a positive correlation with precipitation, albeit insignificant (R^2<0.04, P=0.05). The correlations of both $\delta^{18}O$ and *d*-excess with relative humidity were negligible (R^2=0.02, P<0.01). As relative humidity increased, $\delta^{18}O$ became depleted, while *d*-excess decreased accordingly.

Zhugqu exhibited typical characteristics of high temperature, high relative humidity, and high precipitation (Table 1). Combined with the spatial analysis in Section 3.1, we found that the maximum $\delta^{18}O$ value on the Gannan Plateau occurred at this sampling point, further revealing that the effect of temperature dominated over precipitation and relative humidity in this region. In response to this distinctive phenomenon, we proposed two potential explanations. Firstly, sub-cloud secondary evaporation during precipitation may induce isotope enrichment by modifying the isotopic composition of precipitation. However, on the Gannan Plateau, this effect was modulated by various factors including temperature, precipitation, relative humidity, and raindrop diameter, which consequently attenuated the direct correlation between precipitation isotopes and both precipitation and relative humidity to a certain degree. Secondly, the intricate topography of the Gannan Plateau—characterized by a gradual increase in altitude from east to west—resulted in a pronounced altitude effect that precipitation isotope values declined with increasing altitude.

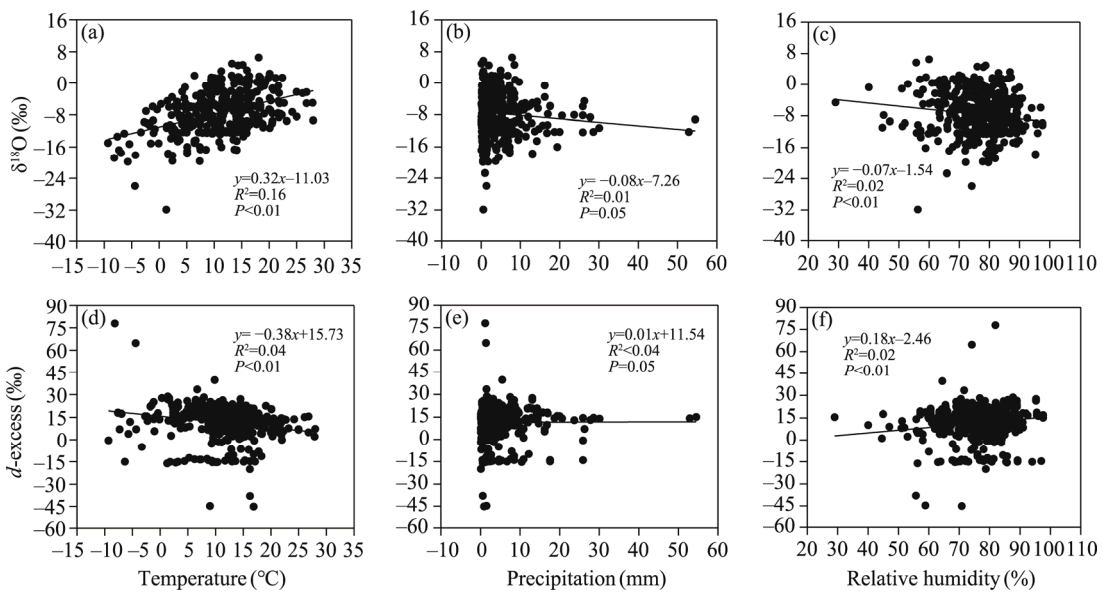

Fig. 6 Correlations of $\delta^{18}O$ and *d*-excess with temperature (a and d), precipitation (b and e), and relative humidity (c and f)

To further investigate the cause of variation in precipitation isotopes on the Gannan Plateau, we conducted an analysis of the relationship between large-scale convective activity and precipitation isotopes within the study area in 2022. Convection and various sources of water vapor are crucial to the process of stable isotope fractionation occurring during monsoon precipitation. The OLR data can offer valuable insights into convection intensity and the positioning of the Intertropical Convergence Zone (ITCZ), with lower OLR values indicating enhanced convection. Figure 7

illustrates that from May to August, alterations in sources of water vapor—driven by both southwest and southeast monsoons—resulted in intensified convection and increased precipitation over the Gannan Plateau, leading to a decrease in $\delta^{18}O$ values. During this timeframe, intensification of the ITCZ over the Bay of Bengal and western Pacific Ocean significantly influenced climatic conditions on the plateau. However, beginning in September, as monsoon activity gradually diminished, there was a reduction in ITCZ intensity alongside a resurgence of subtropical high-pressure systems that restored dominance to northwest-sourced water vapor. This transition resulted in elevated $\delta^{18}O$ values and a cessation of correlation between OLR data and precipitation isotopes on the Gannan Plateau.

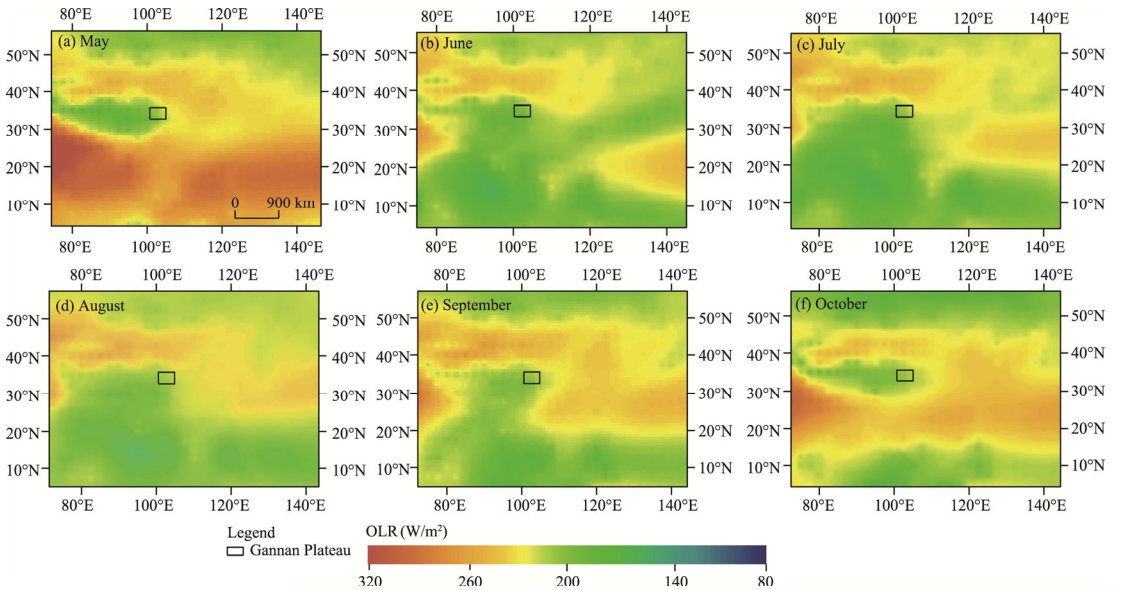

Fig. 7 Spatial variations in outgoing longwave radiation (OLR) in May (a), June (b), July (c), August (d), September (e), and October (f) on the Gannan Plateau

3.5 Tracking potential water vapor sources areas at the sampling points using *d*-excess signals

The trajectory simulated by the HYSPLIT model can only determine the main orientation and location of the water vapor sources of precipitation on the Gannan Plateau (Yue et al., 2022). Through the above tracer study of the water vapor sources on the Gannan Plateau, we found that the contribution of the local circulation water vapor to the precipitation in summer and autumn should not be neglected. Therefore, PSCF and CWT analyses were used to investigate potential water vapor source areas for the five sampling points on the Gannan Plateau from June to November. Figure 8a shows that the high probability areas for Maqu are scattered, and most of them are concentrated near the study area, especially in Linxia Hui Autonomous Prefecture and Wuwei City in Gansu Province of China in the north of Maqu, with high probabilities of more than 0.7. At the same time, there was also a potential water vapor source area with a probability of more than 0.5 in the south of Maqu. Figure 8c shows that the high probability areas for Hezuo were concentrated in the southwest and northwest directions. The high probabilities of Nyingchi City in Xizang Autonomous Region of China in the southwest of Hezuo and Ili Kazak Autonomous Prefecture in Xinjiang Uygur Autonomous Region of China in the northwest of Hezuo were both more than 0.5. In addition, there were also a few high probability areas around the Hezuo, and the probabilities could reach more than 0.3. The results of the PSCF analysis at Têwo were linearly distributed, and only a few high probability areas were located in the southern part of the study area (Fig. 8e). Lijiang City in Yunnan Province, China was the main potential water vapor source area for Têwo with a probability of more than 0.3. It could be seen that the high probability areas for Zhugqu were mainly distributed in the southern direction, and the

southwest and southeast directions had potential water vapor source areas with probabilities of more than 0.7 (Fig. 8g). The high probability areas for Xiahe were relatively concentrated, among which the probabilities of Haidong City in Qinghai Province of China and Jinchang City in Gansu Province were up to 90.00% (Fig. 8i). Ya'an City in Sichuan Province of China in the south of Xiahe and Dingxi City in Gansu Province in the east of Xiahe were also its potential water vapor source. On the whole, the potential water vapor source areas in summer and autumn on the Gannan Plateau were mainly distributed in Yunnan Province, Sichuan Province, Xinjiang Uygur Autonomous Region, and Xizang Autonomous Region in the west and south of the study area.

The results of CWT analysis were similar to those of PSCF analysis, and the distribution areas of high *d*-excess values were basically the same. The contribution rates of potential water vapor sources changed little for Maqu, and no obvious high values were found around the sampling point (Fig. 8b). The areas showing the largest contribution rates were in Linxia Hui Autonomous Prefecture and Wuwei City in the north of Maqu and the rates were more than 8.00‰/m^3. At Hezuo, the contribution rates of the surrounding areas were large. It could be seen that areas with high contribution rates were distributed in the north–south direction, and there were potential water vapor source areas with a contribution rate of up to 18.00‰/m^3 in the northwest and southwest directions (Fig. 8d). The potential water vapor source areas at Têwo were mainly distributed in Wuwei City, Haidong City, Nyingchi City, and Lijiang City, with contribution rates more than 14.00‰/m^3 (Fig. 8f). The contribution rates of potential water vapor source areas for precipitation at Zhugqu were obviously different (Fig. 8h). The high-value areas were concentrated in the vicinity of Zhugqu. The contribution rates of Longnan City and Dingxi City in Gansu Province were all above 9.00‰/m^3, and Nyingchi City in the southeast also existed a high-value area. The potential water vapor source areas for precipitation at Xiahe were concentrated around the study area, especially in Linxia Hui Autonomous Prefecture, Dingxi City, and Tianshui City in Gansu Province, where they were close to each other, with the highest contribution rate of 12.00‰/m^3 (Fig. 8j).

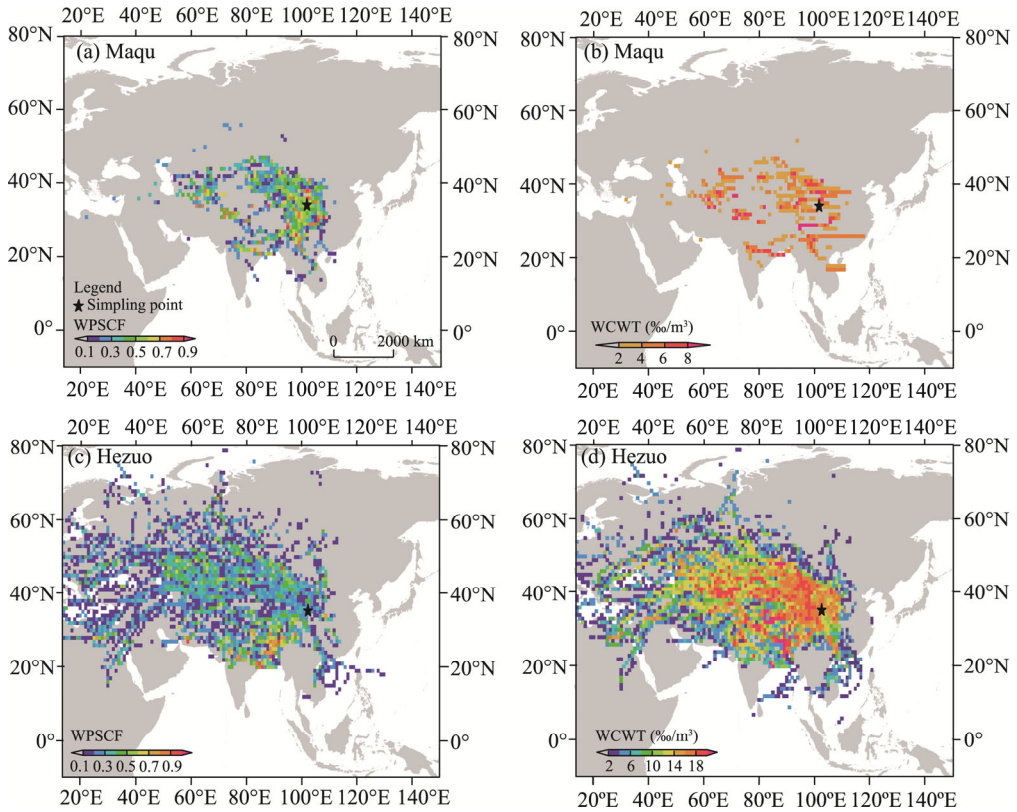

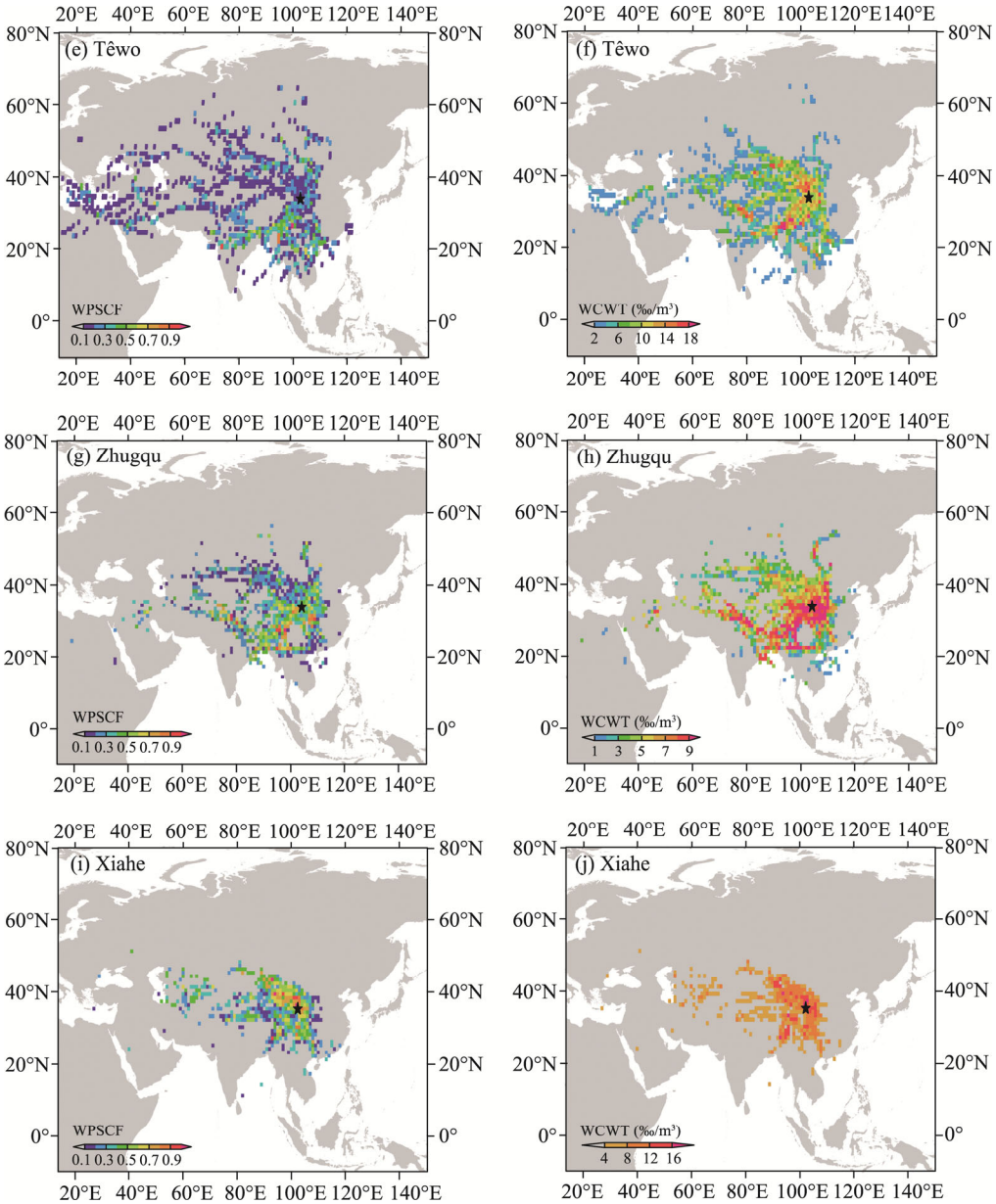

Fig. 8 Results for Potential Source Contribution Function (PSCF) and Concentration Weighted Trajectory (CWT) analyses of potential water vapor sources at Maqu (a and b), Hezuo (c and d), Têwo (e and f), Zhugqu (g and h), and Xiahe (i and j) on the Gannan Plateau in 2022. Note that the base map was obtained from the Meteoinfo website (http://www.meteothink.org/index.html#).

3.6 Isotopic leaching effects and water vapor sources during sustained precipitation events

The variation in precipitation isotopes serves as an indicator of the water cycle patterns. For instance, for the precipitation event at Hezuo from 10 July to 18 July 2022, various factors exhibited distinct changes (Fig. 9). Temperature initially rose before subsequently declining, precipitation isotopes first became depleted and then enriched, relative humidity consistently decreased, while *d*-excess displayed fluctuating trends. The ranges for $\delta^{18}O$ (from –10.29‰ to –1.15‰) and $\delta^{2}H$ (from –46.72‰ to 13.34‰) were substantial, with weighted averages recorded at –6.48‰ and –11.59‰, respectively. Similar phenomena have been documented during continuous precipitation events across other regions as well. Notably, a summer precipitation event characterized by sustained high precipitation at Margate in Tasmania, Australia also

revealed a pronounced depletion of $\delta^{18}O$ (Barras and Simmonds, 2008). Moreover, real-time analyses of ongoing precipitation processes in tropical Australia revealed that $\delta^{18}O$ and $\delta^{2}H$ values exhibited pronounced fluctuations within a single day. These rapid variations were intricately associated with alterations in the sources of water vapor, as well as its transport pathways and historical precipitation patterns (Munksgaard et al., 2012).

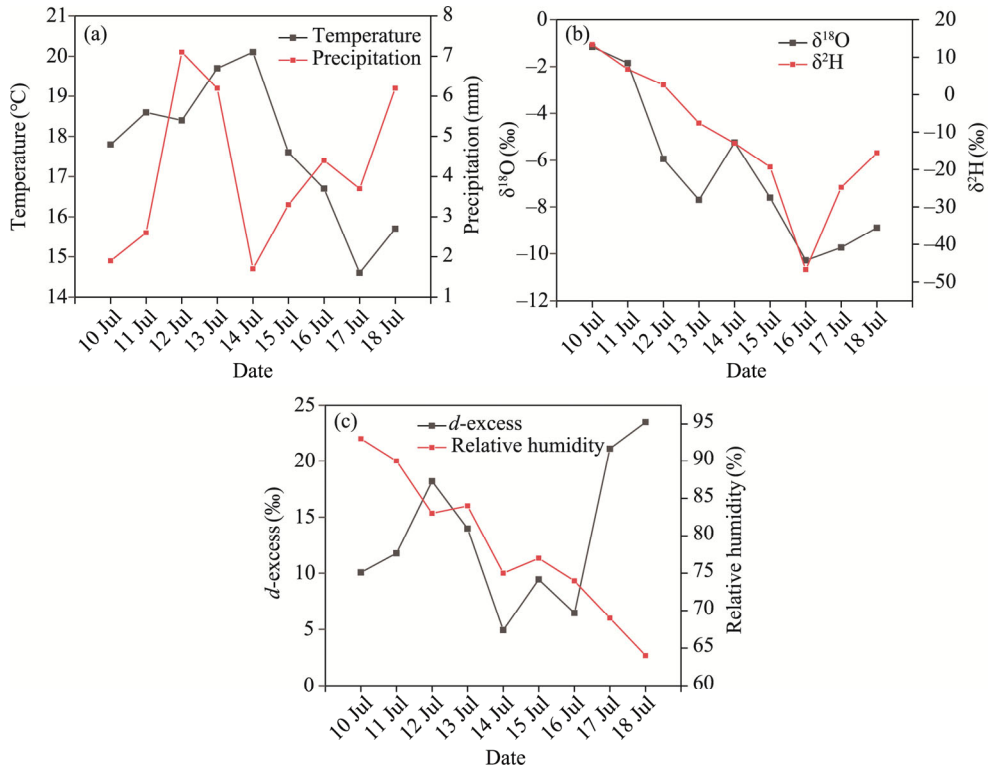

Fig. 9 Variations in precipitation isotopes and meteorological factors during the precipitation event at Hezuo from 10 July to 18 July 2022. (a), temperature and precipitation; (b), $\delta^{18}O$ and $\delta^{2}H$; (c), *d*-excess and relative humidity.

We further used the HYSPLIT model to trace the water vapor transport paths for the precipitation event mentioned above (Fig. 10). The precipitation event could be divided into three stages. During the initial stage (from 10 July to 12 July), when westerly water vapor and local recycled water vapor were the main sources, both temperatures and isotope values were high, indicating a continental air mass. During the middle stage (from 13 July to 15 July), the water vapor transport path shifted southwestward, originating primarily from the Bay of Bengal and South Asia under monsoon influence. This air mass was mixed with water vapor with lower isotope values, while increased precipitation caused further isotope depletion. These characteristics reflected the dominance of a low-latitude oceanic air mass during this period. In the final stage (from 16 July to 18 July), the continuous precipitation event approached its end, with temperature and relative humidity dropping to their lowest levels. During this phase, monsoon water vapor gradually weakened and local recycled water vapor became the main source, with $\delta^{18}O$ and $\delta^{2}H$ values gradually enriching.

Overall, the continuous precipitation process conformed to the Rayleigh fractionation model during stages with the same water vapor source, indicating that during the condensation process of water vapor, water vapor rich in heavy isotopes (^{18}O and ^{2}H) condensed first to form precipitation, while ^{18}O and ^{2}H gradually became depleted in the air mass that subsequently forms precipitation, resulting in gradually negative $\delta^{18}O$ and $\delta^{2}H$ values in precipitation. Similar phenomena have also been observed during continuous precipitation events in the Dunhuang

Basin in Northwest China (Guo et al., 2015). Westerly water vapor, local recycled water vapor, and southwest monsoon water vapor all affected the entire precipitation process, with the initial and final stages mainly influenced by continental air masses, and the middle stage with gradually increasing precipitation mainly controlled by marine air masses.

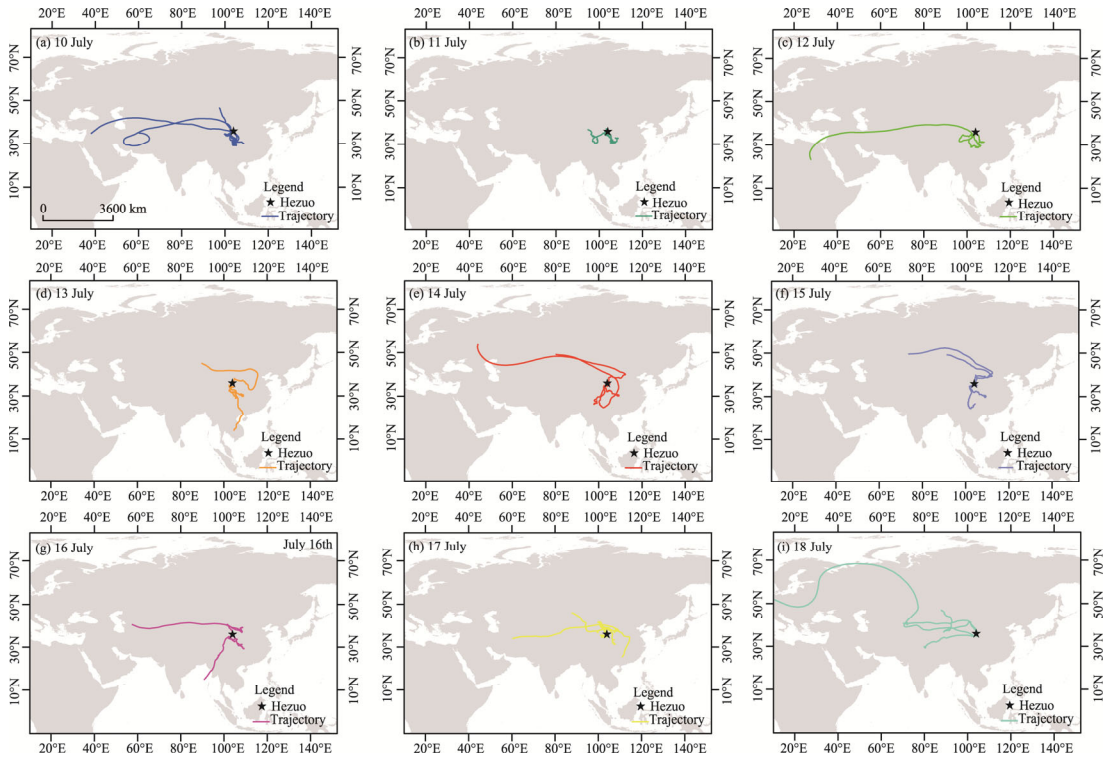

Fig. 10 Backward trajectory tracking of the HYSPLIT modeled persistent precipitation water vapor sources during the precipitation event at Hezuo from 10 July to 18 July 2022. HYSPLIT, Hybrid Single-Particle Lagrangian Integrated Trajectory (HYSPLIT). Note that the base map was obtained from the Meteoinfo website (http://www.meteothink.org/index.html#).

4 Conclusions

In this study, we analyzed the spatiotemporal variation characteristics of precipitation isotopes and their correlations with meteorological factors on the Gannan Plateau. Through backward trajectory modeling combined with PSCF and CWT analyses, we systematically identified the water vapor sources. A case study further revealed precipitation isotopic variations and corresponding water vapor source transitions during continuous precipitation events. The findings indicated that while there were low-high-low distributions of isotopes over spring, summer, and autumn, the overall fluctuation was not statistically significant. On the Gannan Plateau, the spatial variation in $\delta^{18}O$ and $\delta^{2}H$ of precipitation revealed a rising trend from west to east. Compared to the GMWL, the LMWL for precipitation on the Gannan Plateau exhibited a lower slope and intercept, reflecting the presence of below-cloud secondary evaporation effects in the region, which led to the enrichment of stable isotopes ($\delta^{18}O$ and $\delta^{2}H$). Inland water vapor carried by the westerlies and ocean recharge water vapor along the path made up the majority of the continuously water vapor supply on the Gannan Plateau, according to the HYSPLIT model simulation. In addition, monsoon water vapor and local circulation water vapor supplemented in summer and autumn. The primary potential water vapor source areas were located in the western part of the study area. An analysis of a sustained precipitation event on the Gannan Plateau revealed that during the event, high relative humidity and substantial precipitation led to an initial

depletion followed by enrichment of $\delta^{18}O$ and $\delta^{2}H$. The process was divided into three phases: the early stage influenced by westerly air masses and local water vapor sources, the middle stage dominated by water vapor from the Bay of Bengal and the South Asian monsoon, and the final stage when local recycled water vapor became predominant. This study revealed the importance of water vapor transport for water resource management in the arid and semi-arid areas, providing scientific guidance for research on regional water cycle processes. Meanwhile, it also outlines future research directions, including using multi-year precipitation data to conduct in-depth analysis of the complex relationship between isotopic composition and water vapor sources to further improve the accuracy of climate predictions and regional water resource management.

Conflict of interest

The authors declare that they have no known competing financial interests or personal relationships that could have appeared to influence the work reported in this paper.

Acknowledgements

The research is supported by the National Natural Science Foundation of China (42161007), the Innovation Foundation of Higher Education Institutions of Gansu Province (2021B-081), and the Foundation for Distinguished Young Scholars of Gansu Province (20JR10RA112).

Author contributions

Conceptualization: CHEN Fenli, KANG Nan; Data curation: KANG Nan, LI Huizhen, GAO Minyan, YAO Yiwen; Funding acquisition: CHEN Fenli, WANG Shengjie; Methodology: CHEN Fenli, WANG Shengjie; Writing - original draft: CHEN Fenli, KANG Nan; Writing - review & editing: CHEN Fenli, KANG Nan, ZHANG Qiuyan. All authors approved the manuscript.

References

Barras V J I, Simmonds I. 2008. Synoptic controls upon $\delta^{18}O$ in southern Tasmanian precipitation. Geophysical Research Letters, 35(2): L02707, doi: 10.1029/2007GL031835.

Begum B A, Kim E, Jeong C H, et al. 2005. Evaluation of the potential source contribution function using the 2002 Quebec forest fire episode. Atmospheric Environment, 39(20): 3719–3724.

Chen F L, Chen J F, Wang S J, et al. 2022a. Below-cloud evaporation effect on stable water isotopes in precipitation at the eastern margin of Qinghai-Tibet Plateau. Hydrological Processes, 36(10): e14699, doi: 10.1002/hyp.14699.

Chen J F, Chen F L, Wu X X, et al. 2022b. Hydrogen and oxygen stable isotope characteristics and water vapor sources of precipitation over Mongolian Plateau based on LMDZ model. Scientia Geographica Sinica, 42(9): 1654–1664. (in Chinese)

Craig H. 1961. Isotopic variations in meteoric waters. Science, 133(3465): 1702–1703.

Dansgaard W. 1964. Stable isotopes in precipitation. Tellus, 16(4): 436–468.

Guo X X, Feng Q, Li Z X, et al. 2015. Variation of stable isotopes and moisture sources in precipitation at the Dunhuang Basin in Northwest China. Journal of Desert Research, 35(3): 715–723. (in Chinese)

Huang Y M, Song X F, Zhang X P, et al. 2017. Relationship of stable water isotopes in precipitation with ENSO in Dongting Lake Basin. Scientia Geographica Sinica, 37(5): 792–798. (in Chinese)

Kohfahl C, Rodríguez R F, Bermudo F R, et al. 2021. Vapour source and spatiotemporal variation of precipitation isotopes in Southwest Spain. Hydrological Processes, 35(12): e14445, doi: 10.1002/hyp.14445.

Li X X, He H Y, Wang T, et al. 2022. Analysis on temporal and spatial characteristics of short-term heavy precipitation in Zhouqu from 2010 to 2020. Journal of Agricultural Catastrophology, 12(6): 74–76. (in Chinese)

Liu Y X, Wang Y Z, 2023. Ecological sensitivity assessment of Zhouqu county based on resilience concept. Science Technology And Industry, 23(17): 178–183. (in Chinese)

Liu Z F, Tian L D, Yao T D, et al. 2009. Spatial distribution of $\delta^{18}O$ in precipitation over China. Chinese Science Bulletin, 54(6): 804–811. (in Chinese)

Meng H F, Zhang M J, Wang S J, et al. 2020a. Isotopic characteristics of water vapor and its sources during day and night along the Heihe River in summer. Arid Land Geography, 43(2): 360–370. (in Chinese)

Meng H F, Zhang M J, Wang S J, et al. 2020b. Precipitation isotope characteristics and water vapor source analysis in the upper reaches of the Heihe River. Journal of Glaciology and Geocryology, 42(3): 937–951. (in Chinese)

Munksgaard N C, Wurster C M, Bass A, et al. 2012. Extreme short-term stable isotope variability revealed by continuous rainwater analysis. Hydrological Processes, 26(23): 3630–3634.

Shi Y D, Wang S J, Wang L W, et al. 2021. Isotopic evidence in modern precipitation for the westerly meridional movement in Central Asia. Atmospheric Research, 259: 105698, doi: 10.1016/j.atmosres.2021.105698.

Song Y, Wang S J, Zhang M J, et al. 2022. Stable isotopes of precipitation in the eastern Tarim River Basin and water vapor sources. Environmental Science, 43(1): 199–209. (in Chinese)

Sun C J, Zhou S J, Jing Z W. 2023. Variability of precipitation-stable isotopes and moisture sources of two typical landforms in the eastern Loess Plateau, China. Journal of Hydrology: Regional Studies, 46: 101349, doi: 10.1016/j.ejrh.2023.101349.

Tian L D, Yao T D, Sun W Z, 2001. The relationship between δD and $\delta^{18}O$ and water vapor cycle in precipitation over the northern and southern Tibetan Plateau. Science in China (Series D): Earth Science, 31(3): 214–220. (in Chinese)

Wang K L, Jiang H, Zhao H Y, 2005. Atmospheric water vapor transport from westerly and monsoon over the Northwest China. Advances in Water Science, 16(3): 432–438. (in Chinese)

Wang Y Q, Zhang X Y, Arimoto R, 2006. The contribution from distant dust sources to the atmospheric particulate matter loadings at XiAn, China during spring. The Science of the Total Environment, 368(2–3): 875–883.

Wang Y Q. 2014. MeteoInfo: GIS software for meteorological data visualization and analysis. Meteorological Applications, 21(2): 360–368.

Wei N, Gong Y F, Sun X, et al. 2010. Variation of precipitation and water vapor transport over the Northwest China from 1959 to 2005. Journal of Desert Research, 30(6): 1450–1457. (in Chinese)

Wei W, Meng X D, Han B L, et al. 2023. Change trend of main extreme climate indexes in Gannan Prefecture from 1991 to 2020. Journal of Agricultural Catastrophology, 13(6): 101–103. (in Chinese)

Wu X X, Chen F L, Liu X Y, et al. 2021. The significance of hydrogen and oxygen stable isotopes in the water vapor source in Dingxi Area. Water, 13(17): 2374, doi: 10.3390/w13172374.

Yang G H, Wang S J, Zhang M J, 2022. Spatial distribution of $\delta^{18}O$ in precipitation across the Loess Plateau. Journal of Earth Environment, 13(4): 393–404. (in Chinese)

Yu J J, Li Y F. 2018. Uncertainties in the usage of stable hydrogen and oxygen isotopes for the quantification of plant water sources. Acta Ecologica Sinica, 38(22): 7942–7949.

Yuan R F, Jia W X, Li Z X, et al. 2020. Precipitation stable isotope regional difference in Shiyang River basin. China Environmental Science, 40(11): 4945–4956. (in Chinese)

Yue X B, Zhang M J, Wang S J, et al. 2022. Variation characteristics and influencing factors of precipitation isotopes in Lanzhou. Journal of Glaciology and Geocryology, 44(5): 1620–1630. (in Chinese)

Zhang B J, Li Z X, Wang Y, et al. 2019. Characteristics of stable isotopes and analysis of water vapor sources of precipitation at the northern slope of the Qilian Mountains. Environmental Science, 40(12): 5272–5285. (in Chinese)

Zhang M J, Wang S J, 2016. A review of precipitation isotope studies in China: Basic pattern and hydrological process. Journal of Geographical Sciences, 26(7): 921–938.

Zhang W X, Furtado K, Wu P L, et al. 2021. Increasing precipitation variability on daily-to-multiyear time scales in a warmer world. Science Advances, 7(31): eabf8021, doi: 10.1126/sciadv.abf8021.

Zhang Y Y, Xin C L, Guo X Y, et al. 2024. Characteristics of stable isotopes in precipition and its moisture sources in the inland regions of Northwest China. Environmental Science, 45(4): 2080–2095. (in Chinese)

Zhao H Z, He T, Guo R X, et al. 2023. Meteorological drought variation characteristics in the Gannan Plateau based on standardized precipitation evapotranspiration index. Journal of Arid Meteorology, 41(5): 688–696. (in Chinese)

Zhao P, Xu X Y, Qu J J, et al. 2019. Characteristics of D and $\delta^{18}O$ in precipitation in Qingtu lake area, at lower reaches of Shiyanghe river and its water vapor sources. Journal of Arid Land Resources and Environment, 33(3): 80–85. (in Chinese)

Zhou X, Chen F L, Wu X X, et al. 2020. Variation characteristics of stable isotopes in precipitation and response to regional climate conditions during pre-monsoon, monsoon and post-monsoon periods in the Tianshui Area. Water, 12(9): 2391, doi: 10.3390/w12092391.